The effect of laser wavelength on emission and particle dynamics of Sn plasma

D. Campos,[a] S. S. Harilal, and A. Hassanein
School of Nuclear Engineering, Center for Materials Under Extreme Environment, Purdue University, 400 Central Drive, West Lafayette, Indiana 47907, USA

(Received 9 July 2010; accepted 24 August 2010; published online 9 December 2010)

We investigated the effects of laser wavelength on the atomic, ionic, and radiative emission from laser-produced tin plasmas. For generating plasmas, planar tin targets were excited using either high intensity neodymium-doped yttrium aluminum garnet (Nd:YAG, 1.06 μm) or carbon dioxide (CO_2, 10.6 μm) laser pulses; both are considered to be potential excitation lasers for an extreme ultraviolet (EUV) lithography laser-produced plasma light source. Various diagnostic tools were utilized for investigating ionic, neutral, and radiative emission from Sn plasmas including Faraday cup, witness plate in conjunction with x-ray photoelectron spectroscopy (XPS), EUV, and visible emission spectroscopy and photography. Atomic and ionic analysis showed that the amount of debris emitted by the Nd:YAG generated plasmas was considerably higher than the CO_2 laser-produced plasmas. The angular distributions of both atomic and ionic debris were found to be more forward-centric for the 1.06 μm generated plasma while being much more uniform for the 10.6 μm heated plasma. EUV and visible emission images of the plasma also showed a forward-centric appearance for 1.06 μm heated plasmas. The strength of excited neutral emission was considerably lower for the case of the 10.6 μm plasma while the kinetic energies of ions debris were found to be much higher for CO_2 generated plasmas. Surface analysis of the craters created by the lasers showed that the mass ablation rate is 3.6 times higher for Nd:YAG laser generated plasmas compared to CO_2 generated plasmas at maximum EUV emission. © *2010 American Institute of Physics*. [doi:10.1063/1.3493118]

I. INTRODUCTION

As the semiconductor industry approaches the physical limitations of optical lithography for patterning integrated circuits, the community requires a novel technique for manufacturing its product. For the industry to continue at the pace of Moore's law[1] in increasing processor power, a new light source must be developed in the EUV range with extreme cleanness. This source must emit strongly at a wavelength of 13.5 nm; the selection of 13.5 nm is due to the availability of Mo–Si multilayered mirrors (MLMs) which efficiently reflect a 2% bandwidth at 13.5 nm, the so-called in-band region.[2] Laser-produced plasmas (LPPs) have been proposed as the leading light source for the 13.5 nm radiation as a cheaper alternative to highly expensive synchrotron radiation because they have been shown to emit in-band radiation under certain conditions. Much effort has been spent to explore this possibility.[3–8]

Many studies have been conducted to determine which target is ideal for the production of in-band radiation. Studies have found that plasmas created from lithium,[9] xenon,[10] and tin[11,12] targets when heated to the appropriate temperature emit the requisite 13.5 nm light. Among these options, tin plasmas have been shown to yield high conversion efficiency (CE) from laser power to in-band radiation.[11,12] The CE of a LPP depends on several laser (wavelength,[13] intensity,[14] spot size[7]) and target parameters (geometry,[3] mass density[14]). Previously neodymium-doped yttrium aluminum garnet (Nd:YAG) laser excitation was mainly used for producing tin plasmas which yielded high EUV CE.[13,15] It has since been discovered that CO_2 LPPs provide similar or higher CEs, thus establishing CO_2 LPPs as a promising candidate for EUV source development.

For EUVL sources, along with high CE for obtaining maximum brightness, it is also very important to minimize the damage to the condenser optics by plume debris. The exposure of condenser mirror to plasma debris can result in extreme reflectivity losses through neutral deposition and high energy ion-induced sputtering.[16] Therefore, it is essential to limit the production of debris from the plasma and to develop methods for controlling the debris that is produced. It is also important to limit out-of-band (OoB) radiation because heat-loading of the collector optics can result in distortion of surface geometry leading to further reflectivity losses.[17] CO_2 LPPs have been shown to possess a narrower emission profile around 13.5 nm than Nd:YAG LPPs due to lower plasma density and hence reduced opacity.[13] Several studies have been conducted to devise new or to improve upon existing schemes to mitigate and/or decrease debris emission such as: mass-limited targets,[18,19] ambient gases,[20,21] and magnetic confinement.[19,22]

Currently radiation from both Nd:YAG and CO_2 lasers are considered to be promising excitation sources for producing Sn plasmas and hence significant efforts are going into optimizing laser and target parameters to develop efficient and clean EUV light source. Hence it is imperative to have a detailed account of ion and neutral particle emission from

[a]Electronic mail: dcampos@wisc.edu.

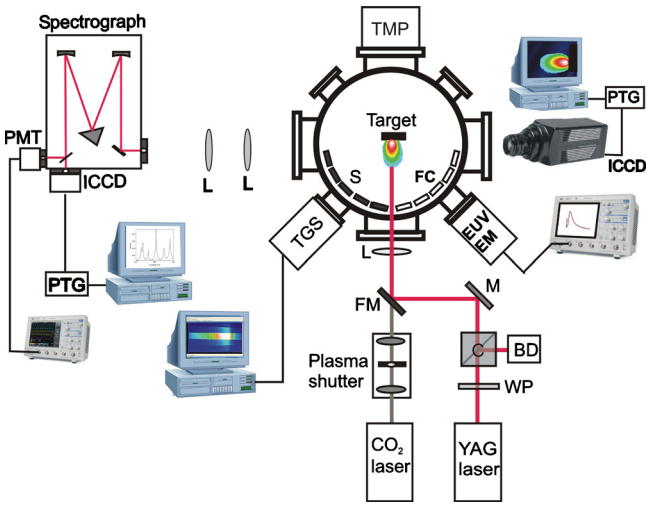

FIG. 1. (Color online) The schematic of the experimental set up is given. (WP, waveplate; C, polarizing cube; BD, beam dump; M, mirror; L, lens; S, substrate; FC, Faraday cup; PMT, photomultiplier tube; ICCD, intensified charge-coupled device; PTG, programmable timing generator; TMP, turbomolecular pump; EUV EM, EUV energy monitor; TGS, transmission grating spectrograph.)

these plasmas for developing efficient debris mitigation schemes. In this article, we report a comprehensive comparison between the atomic and ionic and OoB debris emission from Nd:YAG and CO_2 laser-produced tin plasmas. Our aim is to explore potential advantages of CO_2 versus Nd:YAG LPPs or vice versa for EUV source development.

II. EXPERIMENTAL SET UP

A schematic of the experimental setup is given in Fig. 1. For creating the plasma, radiation from a transversely excited atmospheric CO_2 laser with a 35 ns full width half maximum (FWHM) or pulses from a Nd:YAG laser having 6 ns FWHM was focused onto a planar tin target. The target was mounted on a servomotor controlled XYZ translation stage granting micrometer precision in three dimensions. This mount was placed in the center of a stainless steel vacuum chamber with a base pressure of $\sim 10^{-6}$ Torr. The Nd:YAG laser was attenuated using a combination of a wave plate and polarizing cube. The radiation is then diverted using mirrors and focused onto the target using a f/40 cm quartz lens. The CO_2 laser energy was managed using a simple plasma shutter device which chops the long tail of the CO_2 laser pulses yielding an approximately Gaussian temporal profile and also allows for variable pulse width.[23]

For ionic analysis a Faraday cup (FC) was mounted 17.2 cm away from the laser spot at various angles from the target normal. For atomic debris analysis, silicon witness plates were placed at various angles from the target normal to collect neutral particles. These wafers were then placed in the Interaction of Materials with Particles and Components Testing (IMPACT) (Ref. 16) surface science facility in our center for materials under extreme environment for XPS analysis. The capabilities of IMPACT facility are described in detail elsewhere.[16] A magnesium *K*-α source emitting at 1254 eV was used for the XPS analysis. The atomic fractions were calculated based on the integrated area under the peaks in the spectra using the CASAXPS software package.[24] The areas under the peaks are weighted using the relative intensities of the spectral lines.[25,26]

For the optical emission studies, we employed a 0.5 m spectrograph equipped with an intensified charge-coupled device (ICCD) to characterize the plasma parameters. The spectrograph was equipped with three gratings of 1800 grooves/mm, 600 grooves/mm, and 150 grooves/mm with effective dispersions of 13.1 nm/mm, 3.1 nm/mm, and 0.74 nm/mm respectively. For the EUV spectroscopic studies, we employed a transmission grating EUV spectrograph equipped with a silicon nitride grating (10 000 grooves/mm). For obtaining images of the EUV emission zone, we utilized a pinhole camera equipped with a zirconium filter which captures nearly the entire unresolved transition array (UTA) of tin around 13.5 nm.

We performed the emission spectroscopic studies and imaging analyses in a direction perpendicular to the plasma expansion direction. For obtaining the visible spectrum of the plasmas, we set the ICCD gate to start 100 ns after the onset of the laser pulse with an integration time of 1 μs. ICCD images are used for obtaining plasma expansion features of Nd:YAG and CO_2 generated plasmas. ICCD gates were set at 50 ns and allowed to fire sequentially to obtain a frame-by-frame representation of the plasmas' hydrodynamic expansion.

III. RESULTS AND DISCUSSION

For LPP to be useful for EUV source development, the amount of debris coming from the plasma must be minimized and efficiently mitigated in order to protect the EUV collector optics. This damage results from the energetic ions and neutrals emitted from the plasma plume and heat-loading of the optics caused by OoB emission. LPP is a transient phenomenon which can be divided into three basic parts. First, the laser interacts with the target and excites target materials; electrons are stripped from their atoms and form a sort of plume of electrons and ions. Second, the laser interacts with the plume through the inverse Bremsstrahlung (IB) process and in some cases further ionization. Finally, the LPP cools through adiabatic expansion, Bremsstrahlung radiation, and electron-ion recombination. These steps occur on very short time-scales therefore creating large spatial and temporal variations in plasma properties. Excitation wavelength has a strong influence on the initial two processes (laser-target and laser-plasma interactions). For example, the rate of IB absorption is strongly dependent on laser wavelength (λ), the relation which is approximated by[27]

$$\alpha_{IB} = 1.37 \times 10^{-35}\ \lambda^3 n_e^2 T_e^{-1/2}, \quad (1)$$

where n_e is the electron density and T_e is the electron temperature. Moreover, when the plasma reaches critical density of the pump beam, reflection of the photons by the plasma occurs. Hence the wavelengths of excitation have dramatic effects on the interactions between the laser and the target/plasma as well as the radiative and particle emissions from the resultant plasmas. Our previous studies[3,7,28] showed that the optimum laser pulse parameters for obtaining the highest

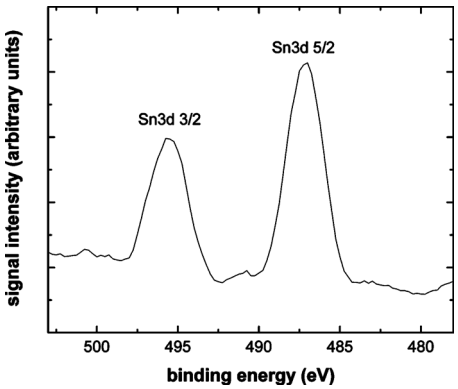

FIG. 2. A sample XPS spectrum of the tin 3*d* peaks. Using these peaks and the silicon 2*p* peak it was possible to calculate the atomic fraction of tin deposited on the wafer surface.

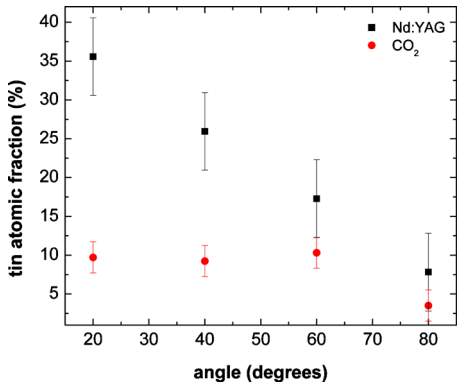

FIG. 3. (Color online) The angular distribution of tin atomic fraction obtained using XPS analysis. The atomic fractions were normalized to a value of 700 shots.

CE for CO_2 (35 ns FWHM) and Nd:YAG (6 ns FWHM) lasers were 6.0×10^9 W/cm^2 and 6×10^{10} W/cm^2, respectively, for a spot size of 225 μm. Hence, we used these laser intensities for the present studies.

A. Atomic and ionic debris analysis

Atomic particles can cause severe damage to MLMs through deposition on the mirror surface. This leads to reflectivity loss of the mirror; therefore, to examine the behavior of atomic emission from the target we placed the silicon witness plates 13 cm away from the laser spot at various angles from the target normal. The tin target was irradiated 700 times by the Nd:YAG laser and 1750 times by the CO_2 laser with two sets of wafers. The difference in number of laser pulses used for the atomic deposition was due to the lower amount of deposition resultant from CO_2 excitation. The calculated atomic fractions CO_2 LPP debris deposited samples were divided by 2.5 to normalize the fractions to a deposition per 700 shots. The samples were all scanned using XPS and thus the atomic fraction of tin on the surface was measured as a function of angle. Figure 2 shows a typical XPS signal of the Sn $3d^{5/2}$ and Sn $3d^{3/2}$ photoelectron peaks. As expected, the ratio of the areas under the peaks is 3:2 which is consistent with the corresponding spin-orbital splitting for 3*d* peaks.[25]

The atomic fractions were compiled as a function of angle and the tabulation is shown in Fig. 3. It is clear from the figure that the amount of atomic debris emitted by the Nd:YAG LPP is considerably higher than that of the CO_2 LPP. Moreover, the shapes of the distributions of debris are markedly different for the Nd:YAG and CO_2 LPPs. There is a large amount of atomic debris emitted in the forward direction from the Nd:YAG LPP. The amount of atomic debris falls off rapidly as the angle from the target normal increases; whereas, in the case of the CO_2 LPP, the distribution is nearly uniform at approximately 10% atomic fraction until much farther away from the target normal.

FCs were employed to record ionic debris features coming from all charge states. The FC provides the kinetic energies of the ions along with ion flux emanating from the plasma. A typical time of flight (TOF) of ion signal obtained with FC is given in Fig. 4 for Nd:YAG and CO_2 LPPs. Three features are readily observable from this figure. First, the amount of ionic debris collected from the Nd:YAG LPP was considerably higher than the CO_2 LPP. This data was obtained simply by integrating the area under the FC signal, in this way we were able to calculate the amount of charge collected. Second, the width of the FC pulse from the CO_2 LPP is considerably narrower than the Nd:YAG LPP's. This implies that there is a higher number of charge-states present in the Nd:YAG LPP. Finally, it is clear that the maximum probably kinetic energy of the CO_2 LPP's ionic debris is higher than that of the Nd:YAG LPP.

The velocities of charged particles emitted from plasmas are governed by space-charge effects. At the onset of the plasma, a wave of electrons is emitted from the target surface at extremely high velocity. These electrons accelerate the positively-charged ions, and because of the nature of the electromagnetic force, more highly-charged ions are accelerated to greater velocities than the lower-charged ions. This implies that ionic debris will travel at a higher velocity compared to the neutral debris and can be implanted into the MLMs thus causing sputtering-induced damage and significant reflectivity losses. It was found that the maximum probable kinetic energy of ionic species from CO_2 LPP is 2.2 ± 0.1 keV which is nearly twice as energetic as the ions emitted from the Nd:YAG LPP which is 1.2 ± 0.1 keV.

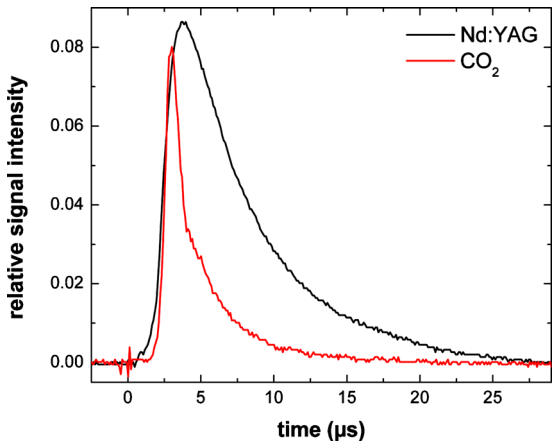

FIG. 4. (Color online) Representative FC TOF profiles from Nd:YAG and CO_2 LPPs.

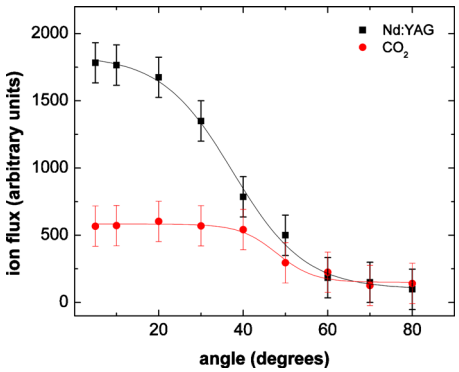

FIG. 5. (Color online) The angular distributions of ionic debris emission of the Nd:YAG and CO_2 LPPs with respect to target normal.

By positioning a FC at various angles throughout the vacuum chamber we were able to construct the angular distributions of the ionic debris emitted by the LPPs. Figure 5 shows that the angular distributions of the ionic debris from the LPPs follow similar trends as their respective atomic debris distributions. For the Nd:YAG LPP, again, there is a high amount of ionic debris emitted in the forward direction; whereas, for the CO_2 LPP the ionic debris distribution is much more uniform. Furthermore, it is clear that the amount of ionic debris emission is considerably higher for the Nd:YAG LPP across the range of angles from the target normal until far away from the target normal where the debris emission is approximately equal.

Previous studies showed that the distribution of ions in a laser created plasma follows single charge dependent $\cos^n$ function where the value of n increases with the charge-state.[29] The ions of the highest ionization state dominate in the direction normal to the target, their concentration falls sharply away from the normal, and excited neutrals have the most angular spread.[29] Our results clearly indicate that the atomic debris has a significantly higher angular spread compared to ionic species in the plasma.

Both neutral and ionic debris showed distinct angular characteristics for Nd:YAG and CO_2 LPPs. These differences are definitely related to initial laser-target and laser-plasma interactions and its wavelength dependence. FC TOF profile provides the distribution of various charge states present in the plasma. Using the estimated kinetic energies from FC TOF signal, we were also able to calculate the average charge-state of ions in the plasmas using the following relation:[30]

$$E(eV) = 5(Z+1)T_e, \tag{2}$$

where E is the most probably kinetic energy, Z is the average charge-state, and T_e is the electron temperature. For the Nd:YAG LPP the average ion charge-state was found to be approximately 8 but for the CO_2 LPP the charge-state was almost 14. These results are in agreement with those published in another work.[31]

The above experiments show that the total atomic and ionic debris emission is clearly higher in the case of the Nd:YAG LPP. This is related to the higher mass ablation rate per pulse from the Nd:YAG laser compared to CO_2 laser. We examined the craters produced by Nd:YAG and CO_2 LPPs

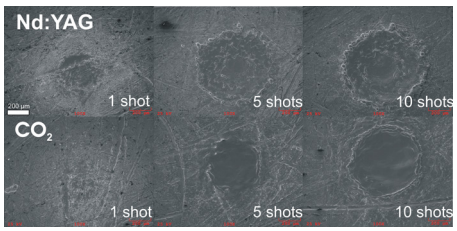

FIG. 6. (Color online) SEM images of the LPP craters on the targets for different numbers of shots (top: Nd: YAG LPP and bottom: CO_2 LPP).

using a scanning electron microscope (SEM) and a surface profilometer. Figure 6 shows SEM images of the craters created by the Nd:YAG and CO_2 lasers for one, five, and ten shots. From the images, it is clear that after just one pulse the Nd:YAG laser there is a noticeable cratering effect; however, the effect is much less pronounced with the CO_2 laser. Furthermore, with more shots fired, there is evidence of splashing and roughness in the Nd:YAG crater whereas with the CO_2 crater the surface is smooth.

In addition to SEM surface imaging, we performed optical surface profilometry. By mapping x and y positions of the crater wall it was possible to construct cross-sectional profiles of the craters. Figure 7 gives cross-sectional mapping of the craters resultant from 10 Nd:YAG and CO_2 laser pulses. The depth of the craters from the surface of the target was found to be 37.7 μm for the Nd:YAG and 14.3 μm for the CO_2. It is clear from Fig. 7 that the shape of the crater can be closely approximated by a paraboloid of revolution. The volume of a paraboloid is given by $V=(1/2)\pi r^2 h$ where r is the radius of the circular "cap" of the paraboloid and h is the axial height of the paraboloid. Using this equation, we calculated the volume of tin displaced from the target. For the craters resulting from ten shots the volumes were found to be 2.9×10^6 μm^3 for the Nd:YAG crater and 0.84×10^6 μm^3 for the CO_2 crater. This gives a ratio of ~3.6. According to Ref. 4, the mass ablation rate of a laser incident on a target is dependent on several factors; this scaling law is given by:[4]

$$\dot{m} \approx (3\times10^3) I_a^{5/9} \lambda^{-4/9} Z_a^{3/8}, \tag{3}$$

where I_a is the laser intensity and Z_a is the atomic number. We calculated the ratio of mass ablation for Nd:YAG pulses versus CO_2 pulses using Eq. (3) which was found to be

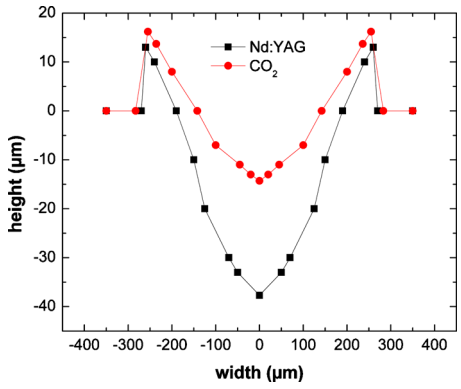

FIG. 7. (Color online) Optical surface profilometry cross-sectional mapping of the LPP craters resultant from ten Nd:YAG and CO_2 laser pulses.

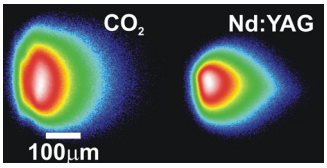

FIG. 8. (Color online) Time-integrated EUV pinhole camera images.

~3.2. This is reasonably consistent with the experimentally measured values. In addition to this, the comprehensive HIGH ENERGY INTERACTION WITH GENERAL HETEROGENOUS TARGET SYSTEMS simulation package predicted that crater resulting from Nd:YAG irradiation is approximately three times deeper than the crater from CO_2 irradiation.[32]

B. EUV imaging and spectroscopic characterization

To examine the underlying causes for the disparities in the debris emission, we performed imaging and spectroscopic studies of the plasmas. Imaging studies allow a better understanding of the hydrodynamic expansion of the plasma and thus the debris distribution, while spectroscopic studies provide a better understanding of radiative emission and thus OoB heat loading to the collector optics. It should be mentioned that highly charged ions (Sn^{8+}–Sn^{13+}) are responsible for emission in the in-band region[5] and lower charged ions and excited neutrals contribute UV and visible emission and this OoB emission contributes heat loading to the collector optics. We imaged the EUV emission zone of the Nd:YAG and CO_2 LPPs using an EUV-sensitive pinhole camera. The camera consists of a 50 μm pinhole with a magnification of ~11. The camera is equipped with a zirconium filter which transmits light of wavelengths between 7 and 15 nm which nearly covers the entire UTA emission of tin plasma.

Representative pinhole images are given in Fig. 8. It is important to note that these images are time-integrated over the lifetime of the plasma which approximately corresponds to laser pulse width. Also, these images are normalized to their respective maximum intensities with the white zone being the most intense. The figure clearly shows a marked difference in the aspect ratios of the EUV emission zones. The forward-centric expansion of the Nd:YAG LPP is clear from the figure, and likewise the more uniform expansion is visible in the case of the CO_2 LPP. This trend mirrors the angular dependence of atomic and ionic particle emission from observed for the Nd:YAG and CO_2 LPPs.

To get a more complete picture of the EUV emission features, we performed EUV spectroscopy. EUV emission spectra from the Nd:YAG and CO_2 LPPs are given in Fig. 9. Immediately evident from the emission spectra is the considerably narrower UTA arising from the CO_2 LPP. Again, in-band EUV emission is the result of excited tin ions ranging from Sn^{8+} to Sn^{13+}, with lower charged ions emitting at higher wavelengths. The Nd:YAG LPP emits a considerable amount of OoB emission on the higher wavelength side which may be due to an enhanced rate of three-body recombination rate arising from its higher electron density.[15]

To get a clearer idea of why the angular distributions of the debris were so different we also performed time-resolved

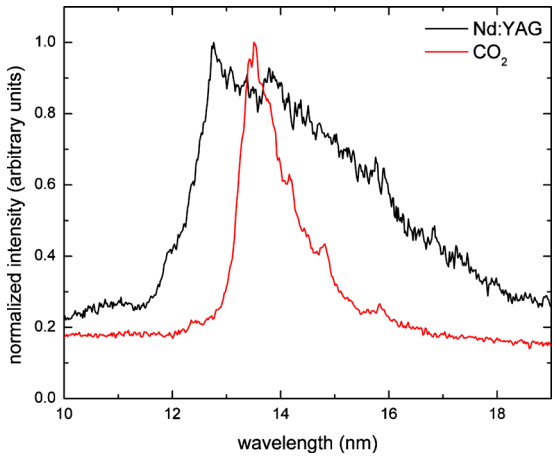

FIG. 9. (Color online) EUV emission spectra for CO_2 and Nd:YAG LPPs.

ICCD imaging of the plasmas. In this way it was possible to observe the hydrodynamic expansion of the plasmas at later times.[33,34] Visible emission from tin plasmas consists of continuum emission from free to free electron transitions (Bremsstrahlung radiation) and line emission originates from excited electrons bound to neutral tin (Sn I) and singly-ionized tin (Sn II).[35] Figure 10 shows the time evolution of the visible emission from the CO_2 and YAG LPPs. Initially, continuum emission dominates over line emission particularly at times <100 ns. After 100 ns, line emission begins to dominate the continuum; however, the continuum emission does not fully disappear until approximately 300 ns. From this, we may infer that the visible emission from roughly the third frame on is the result of excited Sn I and Sn II species. Similar to the EUV images, the CO_2 LPP provides more spherical plume while YAG LPP showed forward centric nature.

Both EUV and visible images were consistent with angular distribution of atomic and ionic species where we observed a relatively uniform distribution of CO_2 LPP debris; whereas the Nd:YAG LPP exhibited a much more forward-centric distribution of debris. From the images it is evident that the Nd:YAG LPP's expansion is more forward-directed than in the case of the CO_2 LPP. Furthermore, it is clear from

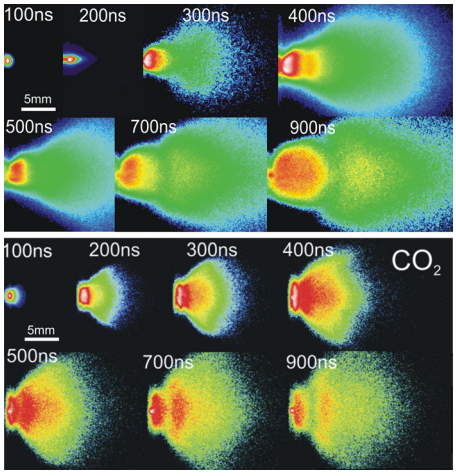

FIG. 10. (Color online) ICCD images of the Nd:YAG and CO_2 LPPs.

the images that the extent of the visible emission is smaller for the case of the CO_2 LPP as observed in our previous studies.[15]

Interferometry studies using a 0.532 μm probe beam from a frequency doubled Nd:YAG laser showed that of the Nd:YAG LPP surpasses the critical density of the probe beam ($\sim 10^{21}$ cm^{-3}) at the peak of the laser pulse while the CO_2 LPP reaches the critical density ($\sim 10^{19}$ cm^{-3}) of the excitation beam.[32] Once the CO_2 LPP reaches the critical density of the pump beam, instead of ablating more target material, the remaining energy of the CO_2 laser pulse is absorbed near the critical density region of the plasma leading to further heating and ionization.[11] This gives rise to enhanced EUV emission despite the lower power density used for CO_2 excitation laser. This localized laser energy absorption near the expanding critical density region explains why the average charge-state of the CO_2 LPP is higher than that of the Nd:YAG LPP. It also explains why the in-band CE of the CO_2 LPP is comparable to (or higher than) that of Nd:YAG LPP despite the large difference in incident laser intensity. It should be remembered that for obtaining the highest CE, ideal plasma temperatures and densities should be created for the longest possible period of time with the maximum size.[32]

The difference in initial densities of the plasmas has a drastic consequence on the expansion dynamics of the respective plasmas. A considerably higher rate of collisional three-body recombination the rate (R_c) of which is given by:[30]

$$R_c \propto Z^3 \ln\sqrt{Z^2+1} T_e^{-9/2} n_e^2 n_i, \quad (4)$$

where Z is the average charge-state, and n_e and n_i are the electron and ion densities, respectively. The enhanced rate of collisional three-body recombination exists in the case of the Nd:YAG LPP due to significantly higher electron density (two orders) compared to CO_2 LPP resulting in increased production of ions with low charge as well as neutral particles farther away from the target.

We also investigated the visible emission characteristics by capturing a visible emission spectrum of the plasma using the ICCD. We manipulated the optics such that the image of the target was 1 mm away from the spectrograph slit. These emission spectra were time-integrated over 1 μs starting from a delay of 100 ns with respect to the incident laser pulses. The purpose of delaying the ICCD gate by 100 ns is for avoiding intense continuum emission during the earliest time of plasma evolution. A trimmed spectrum is given in Fig. 11 for emphasis on the two neutral peaks that are visible in that region. These spectra clearly show that the emission from the neutral lines is considerably stronger in the case of the Nd:YAG LPP when compared with the CO_2 LPP. Also interesting is the prevalence of the CO_2 LPP's relatively stronger continuum emission and weaker line emission which is consistent with our previous work.[15]

The CO_2 LPP showed a higher kinetic energy profile with less flux and the estimated average charge of the plasma is found to be higher (14) compared to YAG LPP (8). It implies that in the case of the CO_2 LPP, more particles escape the target surface without undergoing three-body recombination. The particles which do recombine are emitted more uniformly which can explain why the neutral debris distribution obtained from the XPS analysis shows so little variation for the CO_2 LPP. In the case of the Nd:YAG LPP, the extended recombination zone results in the production of lower-charged ion and neutral debris farther away from the target. Both the visible and EUV spectroscopic studies clearly indicate that three-body recombination plays a significant role in shaping the emission characteristics of the plasmas. Due to the two order of magnitude difference in electron density in the early life of the plasma and much slower decay of density with space,[15] the three-body recombination rate of the Nd:YAG LPP should be much higher at a certain spatial or temporal point during the plasma evolution resulting in enhanced emission at extended regions of the plasma.

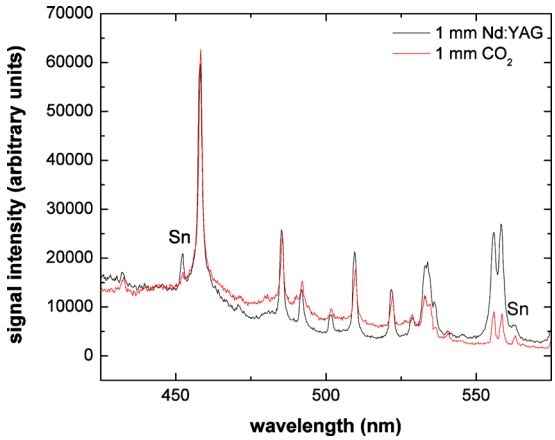

FIG. 11. (Color online) The visible emission spectra of Nd:YAG and CO_2 LPPs taken at 1 mm from the target. The labeled peaks are emission from neutral tin and the unlabeled peaks are emission from Sn^+. The full spectrum was trimmed to 425–575 nm from 374–689 nm to narrow in on the 452.5 and 563.2 nm peaks.

IV. CONCLUSION

We compared atomic, ionic, and radiative emission from Sn plasma produced by Nd:YAG and CO_2 lasers using a multitude of diagnostics tools. It was found through atomic and ionic investigations that considerably more debris is released from a Nd:YAG LPP than from a CO_2 LPP under optimum EUV CE conditions. Moreover, under these conditions it was found that the angular distributions of the debris, both atomic and ionic, were markedly different. The Nd:YAG plasma displayed an extremely forward-centric distribution but the CO_2 plasma showed a more uniform distribution. EUV pinhole and ICCD fast-imaging shed some light on the nature of the hydrodynamic expansion of the two plasmas and showed that Nd:YAG plasma formed a forward biased jet whereas the CO_2 plasma expanded almost spherically which agreed with the debris analysis. Carters created by both laser excitations showed that mass ablation rate is 3.6 times less for CO_2 LPP.

Spectroscopic methods were employed to investigate the in-band and OoB emission characteristics of the plasmas and it was found that collisional three-body recombination plays a strong role in the radiative emission characteristics and

results in considerably more OoB EUV radiation in the case of the Nd:YAG LPP. Also, the recombination rates drastically affect the angular distributions of the plasma debris. It is the extended recombination zone in the Nd:YAG LPP due to its higher density than the CO_2 that results in the drastic differences in the atomic and ionic debris features of the plasmas.

Our results suggest that there are several advantages for using 10.6 μm LPP as a EUVL source versus 1.06 μm LPP. First, with 10.6 μm excitation there is a considerably less atomic and ionic debris emission. The lower rate of collisional three-body recombination in the CO_2 plasma results in the production of a considerably lower neutral population which is evident in the visible emission spectrum. Neutral tin could be the most virulent debris species because it deposits on the surface of the MLMs causing serious reflectivity losses. Though the ionic debris from the CO_2 LPP is found to be more energetic than the ions from the Nd:YAG LPP, the ion flux from CO_2 LPP is found to be substantially lower compared to Nd:YAG LPP. Furthermore, controlling the ionic species is rather easy by using magnetic or electric debris mitigation schemes than manipulating neutral debris and hence minimizing the amount of neutral emission is of paramount importance.

ACKNOWLEDGMENTS

This work was funded in part by Purdue University, College of Engineering. The authors also thank R.W. Coons and Z. Yang for experimental assistance.

[1]G. E. Moore, Proc. IEEE **86**, 82 (1998).
[2]J. M. Slaughter, D. W. Schulze, C. R. Hills, A. Mirone, R. Stalio, R. N. Watts, C. Tarrio, T. B. Lucatorto, M. Krumrey, P. Mueller, and C. M. Falco, J. Appl. Phys. **76**, 2144 (1994).
[3]A. Hassanein, V. Sizyuk, T. Sizyuk, and S. S. Harilal, J. Micro/Nanolith. MEMS MOEMS **8**, 041503 (2009).
[4]R. A. Burdt, S. Yuspeh, K. L. Sequoia, Y. Z. Tao, M. S. Tillack, and F. Najmabadi, J. Appl. Phys. **106**, 033310 (2009).
[5]J. White, A. Cummings, P. Dunne, P. Hayden, and G. O'Sullivan, J. Appl. Phys. **101**, 043301 (2007).
[6]A. Takahashi, D. Nakamura, K. Tamaru, T. Akiyama, and T. Okada, Appl. Phys. B: Lasers Opt. **92**, 73 (2008).
[7]S. S. Harilal, R. W. Coons, P. Hough, and A. Hassanein, Appl. Phys. Lett. **95**, 221501 (2009).
[8]V. Bakshi, *EUV Lithography* (SPIE, New York, 2009).
[9]A. Nagano, T. Mochizuki, S. Miyamoto, and S. Amano, Appl. Phys. Lett. **93**, 091502 (2008).
[10]A. Sasaki, K. Nishihara, M. Murakami, F. Koike, T. Kagawa, T. Nishikawa, K. Fujima, T. Kawamura, and H. Furukawa, Appl. Phys. Lett. **85**, 5857 (2004).
[11]Y. Tao, M. S. Tillack, S. Yuseph, R. Burdt, and F. Najmabadi, Appl. Phys. B: Lasers Opt. **99**, 397 (2010).
[12]S. S. Harilal, T. Sizyuk, V. Sizyuk, and A. Hassanein, Appl. Phys. Lett. **96**, 111503 (2010).
[13]J. White, P. Dunne, P. Hayden, F. O'Reilly, and G. O'Sullivan, Appl. Phys. Lett. **90**, 181502 (2007).
[14]S. S. Harilal, B. O'Shay, M. S. Tillack, Y. Tao, R. Paguio, A. Nikroo, and C. A. Back, J. Phys. D **39**, 484 (2006).
[15]D. Campos, S. S. Harilal, and A. Hassanein, Appl. Phys. Lett. **96**, 151501 (2010).
[16]J. P. Allain, M. Nieto, M. R. Hendricks, P. Plotkin, S. S. Harilal, and A. Hassanein, Rev. Sci. Instrum. **78**, 113105 (2007).
[17]T. Feigl, S. Yulin, T. Kuhlmann, and N. Kaiser, Jpn. J. Appl. Phys., Part 1 **41**, 4082 (2002).
[18]S. Namba, S. Fujioka, H. Sakaguchi, H. Nishimura, Y. Yasuda, K. Nagai, N. Miyanaga, Y. Izawa, K. Mima, K. Sato, and K. Takiyama, J. Appl. Phys. **104**, 013305 (2008).
[19]S. S. Harilal, M. S. Tillack, Y. Tao, B. O'Shay, R. Paguio, and A. Nikroo, Opt. Lett. **31**, 1549 (2006).
[20]S. S. Harilal, B. O'Shay, Y. Tao, and M. S. Tillack, Appl. Phys. B: Lasers Opt. **86**, 547 (2007).
[21]S. Bollanti, P. Di Lazzaro, F. Flora, L. Mezi, D. Murra, and A. Torre, Appl. Phys. B: Lasers Opt. **96**, 479 (2009).
[22]H. Komori, Y. Imai, G. Soumagne, T. Abe, T. Suganuma, and A. Endo, Proc. SPIE **5751**, 859 (2005).
[23]N. Hurst and S. S. Harilal, Rev. Sci. Instrum. **80**, 035101 (2009).
[24]CasaXPS Software Ltd., www.casaxps.com (2009).
[25]M. P. Seah, in *Quantitative Microbeam Analysis*, edited by A. G. Fitzgerald, B. E. Storey, and D. Fabian (The Scottish Universities Summer School in Physics, Great Yarmouth, Norfolk, 1993), p. 1.
[26]S. S. Harilal, J. P. Allain, A. Hassanein, M. R. Hendricks, and M. Nieto-Perez, Appl. Surf. Sci. **255**, 8539 (2009).
[27]J. J. Chang and B. E. Warner, Appl. Phys. Lett. **69**, 473 (1996).
[28]R. W. Coons, S. S. Harilal, D. Campos, and A. Hassanein, J. Appl. Phys. **108**, 063306 (2010).
[29]A. Thum-Jager and K. Rohr, J. Phys. D **32**, 2827 (1999).
[30]P. T. Rumsby and J. W. M. Paul, Plasma Phys. Controlled Fusion **16**, 247 (1974).
[31]R. A. Burdt, Y. Z. Tao, M. S. Tillack, S. Yuspeh, N. M. Shaikh, E. Flaxer, and F. Najmabadi, J. Appl. Phys. **107**, 043303 (2010).
[32]A. Hassanein, V. Sizyuk, S. S. Harilal, and T. Sizyuk, Proc. SPIE **7636**, 76360A (2010).
[33]S. S. Harilal, C. V. Bindhu, M. S. Tillack, F. Najmabadi, and A. C. Gaeris, J. Appl. Phys. **93**, 2380 (2003).
[34]S. S. Harilal, J. Appl. Phys. **102**, 123306 (2007).
[35]Y. Ralchenko, A. E. Kramida, J. Reader, and NIST ASD Team, National Institute of Standards and Technology, 2008.